research papers

Structure-directing sulfur⋯metal noncovalent semicoordination bonding

Ivan V. Ananyev,[a,b]* Nadezhda A. Bokach[c] and Vadim Yu. Kukushkin[c,d]*

[a]Laboratory of X-ray Structural Studies, Institute of Organoelement Compounds (INEOS) of RAS, Vavilova Str., 28, Moscow, 119991, Russian Federation, [b]Department of Chemistry, National Research University Higher School of Economics, Vavilova Str., 7, Moscow, 101000, Russian Federation, [c]Institute of Chemistry, Saint Petersburg State University, Universitetskaya Nab., 7/9, Saint Petersburg, Russian Federation, and [d]South Ural State University, 76, Lenin Av., Chelyabinsk, 454080, Russian Federation. *Correspondence e-mail: i.ananyev@gmail.com, v.kukushkin@spbu.ru

The abundance and geometric features of nonbonding contacts between metal centers and 'soft' sulfur atoms bound to a non-metal substituent R were analyzed by processing data from the Cambridge Structural Database. The angular arrangement of M, S and R atoms with $\angle(R-S\cdots M)$ down to $150°$ was a common feature of the late transition metal complexes exhibiting shortened $R-S\cdots M$ contacts. Several model nickel(II), palladium(II), platinum(II) and gold(I) complexes were chosen for a theoretical analysis of $R-S\cdots M$ interactions using the DFT method applied to (equilibrium) isolated systems. A combination of the real-space approaches, such as Quantum Theory of Atoms in Molecules (QTAIM), noncovalent interaction index (NCI), electron localization function (ELF) and Interacting Quantum Atoms (IQA), and orbital (Natural Bond Orbitals, NBO) methods was used to provide insights into the nature and energetics of $R-S\cdots M$ interactions with respect to the metal atom identity and its coordination environment. The explored features of the $R-S\cdots M$ interactions support the trends observed by inspecting the CSD statistics, and indicate a predominant contribution of semicoordination bonds between nucleophilic sites of the sulfur atom and electrophilic sites of the metal. A contribution of chalcogen bonding (that is formally opposite to semicoordination) was also recognized, although it was significantly smaller in magnitude. The analysis of $R-S\cdots M$ interaction strengths was performed and the structure-directing role of the intramolecular $R-S\cdots M$ interactions in stabilizing certain conformations of metal complexes was revealed.

1. Introduction

A semicoordination bond (SB), the noncovalent analog of the coordination bond, is uncommon but recognized, particularly for metal centers with labile coordination numbers, such as copper(II). This phenomenon (which is also relevant to the so-called *regium* and *spodium* bonding patterns involving transition metal centers (Alkorta *et al.*, 2020) is much less extensively studied than the typical coordination bond, with only *ca* 80 references returned using the query 'semicoordination bond' in CAS SciFinder, compared to 100 000 for 'coordination bond' (CAS SciFinder, February 20th, 2020). The term 'semicoordination' ('semi-co-ordination' in the original spelling) was introduced by Brown *et al.* (1967). They studied the structure of the copper(II) complex $[Cu(en)_2](BF_4)_2$, verified weak Cu⋯F contacts and defined these interactions as semicoordination or 'intermediate type of bonding between coordination and nonbonding, very weakly coordinated'. This bonding was considered a limiting case of axial elongation of the Cu coordination octahedron for compounds of the type

Noncovalent semicoordination bonding
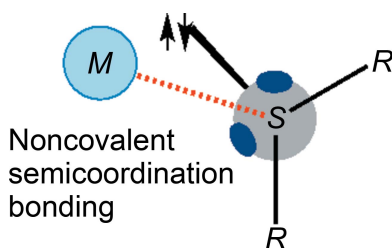
[Cu(NH$_3$)$_4$]X_2 that manifested in unusually long Cu$\cdots X$ distances (Tomlinson *et al.*, 1969). Despite the significant Cu$\cdots$F separation, the contact affects IR spectra of the complexes and this observation led to the conclusion of a slight distortion of BF$_4^-$ and thus the existence of weak Cu$\cdots$F bonding.

Valach *et al.* (Valach, 1999; Valach *et al.*, 2018) applied the bond valence approach to SBs in copper complexes bearing *N*- and *O*-donor ligands. This approach is based on an analysis of experimental structural correlations and involves the computation of the copper(II) atom bond valence as a function of the sum of bond lengths around a metal center. Accordingly, the distances of an SB range from 3.07 Å (for Cu$\cdots$N) to 2.78 Å (Cu$\cdots$O), depending on the interacting atoms. Below these values, the *N*- and *O*-donor ligands are considered bound to the copper center, while at values greater than these distances, the neighboring groups are not bound to each other. An SB, albeit very weak, still might affect the properties of the complexes. In particular, Nelyubina *et al.* (2013) postulated that rather long and weak interatomic contacts [Cu$\cdots$O 3.6 Å, 0.5 kcal mol^{-1} (1 kcal mol^{-1} = 4.184 kJ mol^{-1}); ΣR_{vdw} Cu+O = 2.92 Å] may still mediate magnetic super-exchange pathways, confirming the existence of weak interactions, even at this distance.

Currently, an SB is considered a type of weak attractive noncovalent interaction between an electrophilic region associated with a metal center and a nucleophilic region associated with a nonmetal atom in another or in the same molecular entity (Efimenko *et al.*, 2020). The comparison of the $M\cdots X$ distance with the sum of the corresponding van der Waals radii might serve as a simple initial criterion for the identification of an SB: the $M\cdots X$ distance should be smaller than the sum of the van der Waals radii, but significantly (taking into account the 3σ criterion) longer than the typical coordination bond for the same formal oxidation states of both *M* and *X* (Efimenko *et al.*, 2020). This criterion is not the only one and other methods may also be applied to recognize an SB and distinguish it from other types of noncovalent interactions.

The second approach considers the angles around the *X* and *M* centers; however, the angle potentially depends on the identity of interacting atoms, their valence and directionality. Other approaches that increase the reliability of the SB recognition are based on theoretical calculations and include the estimate of forces involved in the formation of the contact (through an energy decomposition analysis) and identifying the bond path connecting *M* and *X*, a bond critical point (BCP) between *M* and *X* (on the analysis of the electron density topology), and the binding energy. In addition, a comparison of some spectral characteristics with and without SBs might provide additional evidence of the noncovalent interaction.

Based on the data considered above and our search of CAS SciFinder for references that contain the concept 'semi-coordination bond', most studies focused on SB examined copper(II) complexes featuring relatively hard *N*- and *O*-donor ligands. Fewer studies have examined the involvement of other types of ligands, *e.g.* soft *S* ligands, in SBs. However, due to the great abundance of metal species bearing *S*-donor ligands and the number of studies analyzing complexes with sulfur donor ligands, not surprisingly, some examples of weak coordination (or, using the terminology of the present study, SB) of *S*-donors with metal centers have been reported.

Thus, weak Cu$\cdots$S coordination [or SB; 3.144 (1) Å; ΣR_{vdw} Cu+S = 3.2 Å] was identified in the crystal structure of a copper(II) 1,3-dithiole-2-thione-4,5-dithiolate complex; this SB affects the magnetic properties of the complex (Starodub *et al.*, 2012). Similar elongation [Cu$\cdots$S 2.940 (1) Å] was detected in the structure of a copper(II) complex (mimicking the active sites in dopamine β-hydroxylase) with an NSO-donating Schiff base ligand (Santra *et al.*, 2002). Weak Ni$\cdots$S coordination [2.787 (3) Å; ΣR_{vdw} Ni+S = 3.43 Å] at the axial position was recognized in the structure of a square-pyramidal nickel(II) complex (Nakane *et al.*, 2009), the Au$\cdots$S interactions [3.4648 (14) and 3.5384 (14) Å; ΣR_{vdw} Au+S = 3.46 Å] were described for phosphine gold(I) thiolates (Ho *et al.*, 2006), and weak Ag$\cdots$S interactions (2.916–3.197 Å; ΣR_{vdw} Ag+S = 3.52 Å) were observed between adjacent macro-metalacycles of silver(I) pyridyl dithioether complexes (Xie *et al.*, 2004).

In the present study, by processing and inspecting the structures accumulated in the Cambridge Structural Database, we verified various noncovalent sulfur$\cdots$metal contacts and analyzed their abundance, depending on the identity of metal center and its position in the periodic table (Section 2.2). For selected structures of metal complexes with shorter R—S$\cdots M$ contacts, we conducted a theoretical analysis (Section 2.3) and provided insights into the nature of the corresponding interactions, their geometric features and energetics.
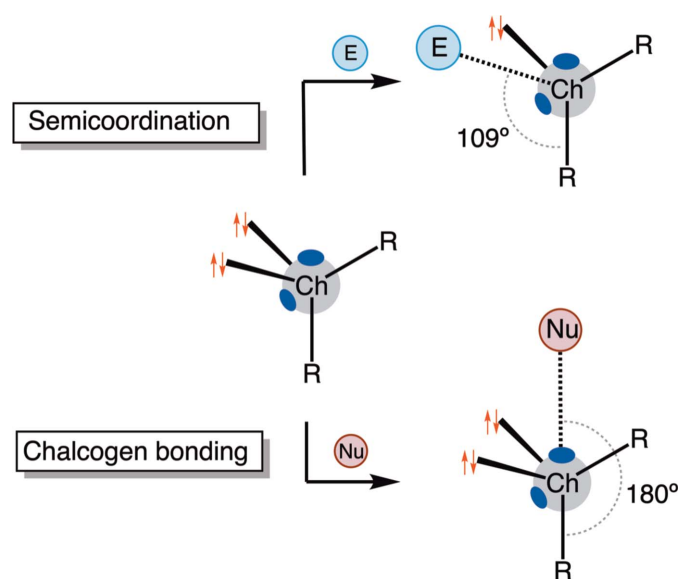
Figure 1
Electrophilic (two σ-holes in blue) and nucleophilic sites (two LPs in red) in ChR_2; formation of a noncovalent contact (SB or HB) with an electrophile and noncovalent contact (ChB) with a nucleophile. The idealized angles are shown for both types of contacts.

In addition to the identification of SBs between sulfur and metal centers (Fig. 1, top panel), we also attempted to answer the question of whether the lone pairs (LPs) of metal centers (even positively charged) are sufficiently nucleophilic to form a chalcogen bond (ChB) with an S-containing center involved in covalent bonding with non-metal atom R and acting as a σ-hole donor (Fig. 1, bottom panel). In other words, does ChB provide a noticeable contribution to the total energy of an $R—$S$\cdots M$ interaction?

In this context, the possibility of electron density anisotropy of soft [in terms of the HSAB principle (Pearson, 1963)] centers should be considered. In the ligated species, soft interacting atoms typically feature both electrophilic and nucleophilic regions, and in addition to the electron-donating ability of their LPs, these centers function as σ- and π-hole donors (Fig. 1). For ChR_2 (Ch = S, Se, or Te), the existence of two nucleophilic and two electrophilic sites has been proven (Scheiner et al., 2020; Scilabra et al., 2019; Vogel et al., 2019), and the directionality of either a pure electron-donating or pure electron-withdrawing interaction is determined by the position of these sites, which in turn determine an optimal interaction angle.

2. Results and discussion

2.1. Semicoordination and chalcogen bonding and theoretical approaches for their evaluation

SBs and ChBs should be considered as opposite interactions based on their directionality to analyze various sulfur$\cdots$metal noncovalent contacts and to estimate the contributions of different forces to an $R—$S$\cdots M$ interaction. Therefore, this section describes approaches for the identification of semicoordination bonds (Section 2.1.1) and chalcogen bonds (Section 2.1.2).

2.1.1. Semicoordination bonding. While the attractive interactions between the transition metal atom and electron-donor non-metal centers are usually described as coordination bonds, their strength varies substantially, spanning a range from a few to dozens of kcal mol^{-1} (Cottrell, 1958; Darwent, 1970; Benson, 1965; Kerr, 1966). This diversity has been observed even within the same metal coordination polyhedron that requires a clear classification of these interactions to describe bonding situations and form reasonable predictions of the structure and properties of a studied system. The accounting of weak coordination bonds, often treated as semicoordination, might be important for estimating the contributions into crystal lattice energy and for the rationalization of relative polymorph stability [for instance, see Bikbaeva et al. (2017), Valach (1999), Wikaira et al. (2017), Awwadi et al. (2011) and Ananyev et al. (2013)]. Despite the absence of a formal definition of 'semicoordination bonding', it usually implies the noncovalent nature of corresponding interactions with the major contribution derived from electrostatics and minor contributions from charge polarization and charge transfer (CT) (Efimenko et al., 2020). This

decomposition implies the geometric preferences of semi-coordination bonding.

The difference between conventional and weak coordination bonds is usually identified using basic structural criteria. Namely, the $M\cdots X$ distance (M is a metal and X is an electron-donor atom) is expected to be nonbonding but short for the semicoordination, i.e., it should be significantly longer than the sum of suitable covalent radii, while still being smaller than the sum of the appropriate Bondi (1966) vdW radii (ΣR_{vdW}). As charge and energy decomposition analysis data are not always available and the vdW radii of metals are statistically valid only in a few cases, various theoretical methods are commonly used to discriminate the interactions of metal atoms (Efimenko et al., 2020; Bikbaeva et al., 2017).

Among those methods, the analysis of real-space fields describing features of the charge distribution comprises one of the most powerful methods (Popelier, 2016; Lyssenko, 2012). The most common real-space method, the Quantum Theory of Atoms in Molecules (QTAIM) (Matta & Boyd, 2007), provides an opportunity to explore bonding diatomic interactions with meaningful exchange energy contributions and subsequently to construct the atomic connectivity graph. The properties of corresponding descriptors of topological bonding, such as interatomic surfaces and $(3, -1)$ critical points (CPs) of electron density $\rho(\mathbf{r})$, serve as weights of the connectivity graph and are frequently used to provide a range diatomic interactions in terms of charge separation and contributions to the energy of the system (Bader & Essén, 1984; Cremer & Kraka, 1984; Silva Lopez & de Lera, 2011; Ananyev & Lyssenko, 2016; Alkorta et al., 1998; Espinosa et al., 1998; Vener et al., 2012; Bartashevich, Matveychuk et al., 2014; Saleh et al., 2015; Lane et al., 2017; Ananyev et al., 2017; Borissova et al., 2008; Romanova et al., 2018). For instance, the topographic analysis of $\rho(\mathbf{r})$ in the transition metal complexes usually indicates the $M\cdots X$ bonding interaction for any coordination bond, i.e. the presence of a $(3, -1)$ $\rho(\mathbf{r})$ CP and corresponding bond path between M and X nuclei. According to the QTAIM analysis, most noncovalent interactions, including semicoordination bonds, are of the closed-shell type, which corresponds to a pronounced electronic charge depletion between atoms supported by the predominant kinetic energy of electrons in this area [at corresponding CPs, $\nabla^2\rho(\mathbf{r}) > 0$, full energy density of electrons $h_e(\mathbf{r}) > 0$]. In contrast, conventional coordination bonds usually correspond to the so-called intermediate type of interaction [at the CP, $\nabla^2\rho(\mathbf{r}) > 0$, $h_e(\mathbf{r}) < 0$]. Notably, due to the uncertainties in the calculations of the $h_e(\mathbf{r})$ values, this criterion is as formal as the geometric criterion and only describes the favorability of electrons to be located between two atoms – the extent of the covalent contribution that is always observed. Further classification of interactions is achieved by picturing CT channels in the real space from fields indicating charge concentrations and depletions, such as $\nabla^2\rho(\mathbf{r})$ and the electron localization function (ELF) (Shaik et al., 2015). Thus, together with the other real-space and orbital approaches for the study of CTs and energies of noncovalent interactions (including widely known charge/energy decomposition schemes such as natural

bonding orbitals (Carpenter & Weinhold, 1988; Foster & Weinhold, 1980; Reed & Weinhold, 1983; Reed *et al.*, 1985, 1988), symmetry-adapted perturbation theory (Jeziorski *et al.*, 1994), interacting quantum atoms (Blanco *et al.*, 2005), *etc.*, the real-space methods provide valuable insights into the nature of semicoordination bonds.

2.1.2. Chalcogen bonding. The IUPAC definition of the chalcogen bond (ChB) is completely consistent with the definitions of other σ-hole (σh) noncovalent interactions (Aakeroy *et al.*, 2019). The ChB donors should possess a pronounced electrophilic site(s) to be attractively bound by suitable nucleophile(s). The location and potential of effective positive-charge sites, similar to halogen bonds (XBs), is obviously governed by the nature of the Ch atom and affected by its covalent environment. In this regard, the structural features of any noncovalent σh interaction are similar. For strong $D \cdots A$ interactions (D and A are, respectively, the donor and acceptor of a σh), the corresponding distance is usually shorter than the sum of the appropriate Bondi vdW radii (ΣR_{vdW}), while $\angle(R-D\cdots A)$ tends to be 180°, providing the most effective electrostatic attraction and the most significant electronic charge transfer (CT) between the nucleophilic and electrophilic sites (Politzer *et al.*, 2017). In addition to the comparison of basic geometric descriptors, the real-space methods mentioned above have been successfully used to identify ChBs and other bonding noncovalent interactions (Minkin, 1999).

However, the specific features of the charge density distribution of the most commonly utilized ChB donors, such as sp^3-hybridized Ch atoms, might affect the $D \cdots A$ interaction to provide deviations from the geometric and CT preferences of ChB. For instance, in contrast to XBs (where the electrophilic site of a donor atom is formally perpendicular to the toroidal electron charge concentration produced by lone electron pairs, LPs), the two LPs of a Ch atom limit the accessibility of electrophilic sites located at the continuations of $R-D$ covalent bonds (Fig. 1). This arrangement of electrophilic and nucleophilic sites on the Ch atom prevents the formation of a pure ChB by providing the possibility for other channels of CT involving chalcogen LPs (Muller, 1994).
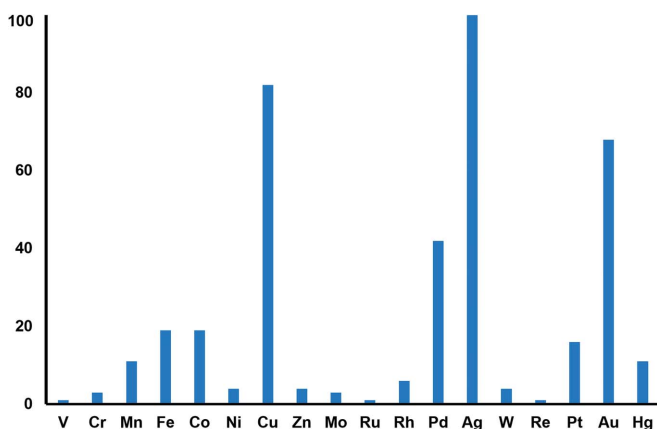
Commonly, the description of two-center bonds for non-metal systems in terms of only one CT channel (the most energetically favorable) provides a satisfactory rationale. Based on the widely known nucleophilic character of Ch atoms in low oxidation states, the interactions involving LPs are also sought first when the secondary bonding of Ch atoms is to be analyzed. Thus, the geometric directionality of an LP(Ch) onto some electron-poor atom (or an atom with electrophilic sites) is often a sufficient condition to classify the Ch atom as a σh acceptor involved in a noncovalent interaction, or as an electron-donor atom participating in a (weak) coordination bond with a metal center. Regarding the possible interplay between different routes of CT, the latter is particularly interesting to consider from the perspective of possible ChB-like CT. The dichotomy of sites of effective charge of Ch atoms, if they are tuned, may provide novel abilities to accurately modulate the electronic properties of metal-containing species.

2.2. CSD data processing and identification of model species exhibiting $R-S\cdots M$ short contacts

2.2.1. Criteria for the CSD data processing and verification of trends. In this study, we analyzed some models chosen by our processing of the Cambridge Structural Database (CSD) (Groom *et al.*, 2016). This search was conducted for crystal structures of transition metal-containing species that are involved in an intra- or intermolecular $R-S\cdots M$ nonbonding contacts with the $S\cdots M$ distance being shorter than the sum of the Bondi vdW radii (Batsanov, 2001; Bondi, 1966) ΣR_{vdW} and $\angle(R-S\cdots M) > 150°$. These restrictions were applied to identify systems with a significant ChB-like CT contribution, even for sulfur as the most nucleophilic chalcogen. The complexes for the theoretical studies were chosen based on the statistical analysis and by considering that these species contain metal centers exhibiting different degrees of the nucleophilicity of LPs at metal centers (*e.g.* Ni, Pd, Pt and Au). The variation in the nucleophilicity is useful for verifying the effect of the identity of metal center on the nature of $R-S\cdots M$ interactions. The presence, character and contributions

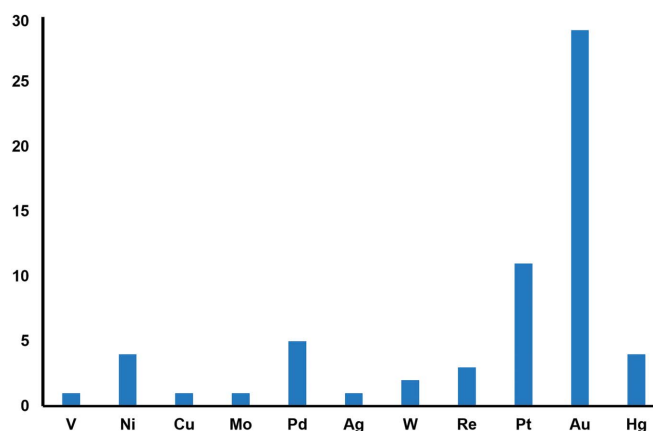**Figure 2**
The distribution of types of metal atoms involved in shortened intramolecular $R-S\cdots M$ contacts according to the CSD search.

Figure 3
The distribution of types of metal atoms involved in shortened intermolecular $R-S\cdots M$ contacts according to the CSD search.

Ananyev *et al.* • Structure-directing S⋯M noncovalent semicoordination bonding　**439**

of $R-$S$\cdots M$ interactions were further analyzed in the chosen examples based on a number of real-space and orbital descriptors.

The processing of the CSD data revealed only 436 structures displaying $R-$S$\cdots M$ nonbonding contacts (R is any non-metal and non-hydrogen atom, while M is a transition metal). In comparison, we identified 28 687 references for an RS fragment and a transition metal. Despite the small number of examples (less than 1.6%), we were able to draw a few preliminary conclusions. In most of the analyzed structures, the sulfur atom forms two single bonds with non-metal atoms, while the R atom at the opposite site of sulfur is the carbon atom in 90% of the $R-$S$\cdots M$ moieties.

In the vast majority of the relevant structures, the $R-$S$\cdots M$ contact is an intramolecular contact (512 fragments in 381 structures), while only 62 intermolecular $R-$S$\cdots M$ contacts in 55 structures were verified. Unfortunately, the rather small amount of data on intermolecular contacts does not allow us to obtain solid statistical conclusions. The small number of examples probably collaterally suggest the relatively insignificant strength of possible $R-$S$\cdots M$ intermolecular interactions with respect to other crystal packing forces. Hence, the usage of metal-involving ChB interactions for controlled supramolecular aggregation is questionable based on the available structural data. Nevertheless, the comparison of these intermolecular contacts with more common intramolecular contacts might provide useful insights, even for the currently available data.

The initial distribution of metal atom types in the structures displaying intramolecular $R-$S$\cdots M$ contacts is significantly affected by the presence of a large fraction of frequently studied cyclopentadienyl and carbonyl metal complexes. The distribution of metal atom types for the remaining 397 intramolecular $R-$S$\cdots M$ contacts (283 structures) is consistent with the general views on the formal nucleophilicity of metal LPs (Fig. 2). Within the same period, the number of relevant structures increases as the charge of the atomic nuclei increases and is maximal for Group 11 (82, 102 and 68 contacts for Cu, Ag and Au complexes, respectively). Because a larger number of structural data are available for 3d metal compounds (e.g. in 53% of structures containing $R-$S$\cdots M$ fragments, M is a 3d metal) the Pd and Pt complexes are the
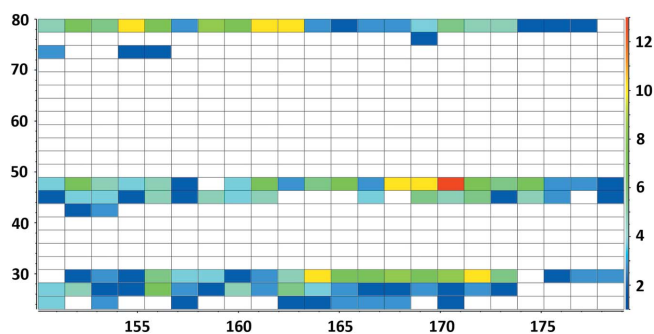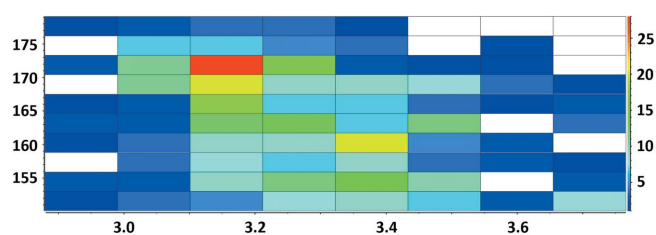
second most common type of structures with intramolecular $R-$S$\cdots M$ contacts (42 and 16 $R-$S$\cdots M$ fragments, respectively). Using the criteria described above, we only identified four relevant nickel complexes featuring $R-$S$\cdots M$ fragments, and this small number of structures deviates slightly from our expectations. However, the expected tendencies were observed for crystals with intermolecular $R-$S$\cdots M$ contacts (Fig. 3). Although the majority of 62 observed contacts were identified for 5d metal complexes in the latter case, the largest fractions are again observed for the metal species for Groups 10 and 11.

The metal coordination number is not more than 4 in approximately 80% of structures with intra- or intermolecular contacts. A more accurate inspection of all these structures revealed the predominance of linear, triangular and square-planar metal coordination, which are common for late transition metals. The structural availability of metal nucleophilic sites in these environments supports the geometric preferences of possible $R-$S$\cdots M$ interactions.

Indeed, the distribution of $\angle(R-$S$\cdots M)$ reveals the possibility for atoms to be arranged in a more linear manner in late transition metal complexes (Fig. S1 in supporting information). At the same time, the modes of distributions of angles within a period deviate significantly from 180° (see the corresponding heat plot in Fig. 4): the mode of the whole distribution of $\angle(R-$S$\cdots M)$ for intramolecular contacts does not exceed 171° and corresponds to Ag and Pd complexes. A small $\angle(R-$S$\cdots M)$ for intramolecular contacts was also observed for late transition 3d metal-containing systems. Notably, the corresponding value for late transition 5d metals is even smaller ($<$163°), indicating a significant number of structures featuring nonlinear $R-$S$\cdots M$ contacts. This finding is even more pronounced for systems with intermolecular contacts, where the mode value for 5d metal complexes is less than 157° (Fig. S2).
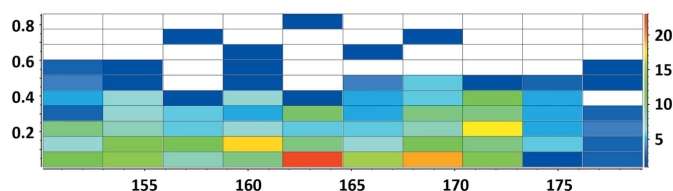
Finally, the S$\cdots M$ distance should be analyzed for at least a qualitative comparison of the strength of an assumed $R-$S$\cdots M$ interaction with its directionality. As the S$\cdots M$ separation strongly depends on the position of the metal in the group, it should not be unambiguously compared with the $\angle(R-$S$\cdots M)$ of intermolecular contacts because of their skewed distribution (Fig. 3). The interrelation of $\angle(R-$S$\cdots M)$ on S$\cdots M$ distances within a period was explored by analyzing structures with intramolecular contacts. Thus, the

Figure 4
Heat plot of the nuclear charge (vertical axis, Ze) of a metal atom versus the $\angle(R-$S$\cdots M)$ (horizontal axis, °) in systems with intramolecular $R-$S$\cdots M$ contacts. The cell color denotes the distribution density.

Figure 5
The heat plot of the $\angle(R-$S$\cdots M)$ (vertical axis, °) versus the S$\cdots M$ distance (horizontal axis, Å) in systems with intramolecular $R-$S$\cdots M$ contacts. The cell color denotes the distribution density.

heat plot of $\angle(R-S\cdots M)$ against the $S\cdots M$ distance shows that smaller distances (more typical for late transition metals) may favor a more linear arrangement of R, S and M atoms (Fig. 5). This trend, however, is not confirmed by the analysis of the heat plot of $\angle(R-S\cdots M)$ against the difference between the $S\cdots M$ distance and appropriate value of ΣR_{vdW} (Fig. 6). Compared with the $S\cdots M$ distance, the latter difference is less dependent on the nature of the metal atom and may serve as an arbitrary measure of the strength of the interaction. Although we identified a relatively large number of structures with shortened intramolecular contacts and high $\angle(R-S\cdots M)$ (see bars at ~173° in Fig. 6), the largest shortening and the largest distribution density are observed for an $\angle(R-S\cdots M)$ equal approximately to 162°. From the small amount of available data for intermolecular contacts (Fig. S3), we also assumed that smaller $\angle(R-S\cdots M)$ are even more favorable for more shortened contacts. The shortening of intramolecular contacts is in general more pronounced (maximal shortening of ~0.85 Å versus ~0.50 Å for intermolecular contacts). This finding is rationalized by the restraints imposed on $R-S\cdots M$ contacts by covalent bonds within a molecule and indicates structural flexibility, which is the inherent feature of weak interactions.

2.2.2. Model structures exhibiting $R-S\cdots M$ contacts. The statistical trends analyzed in Section 2.2.1 indicate that the short $R-S\cdots M$ contacts with $\angle(R-S\cdots M) > 150°$ are usually observed in structures of the 10th and 11th groups of metals in low oxidation states. Based on the formal perspective outlined in Section 2.1.2, $R-S\cdots M$ contacts of the nucleophilic metals (or, in other words, with the expressed Lewis basicity) with these large $\angle(R-S\cdots M)$ might be a manifestation of ChBs. However, despite the restrictions imposed on $\angle(R-S\cdots M)$ in the CSD search, our analysis revealed a tendency of $R-S\cdots M$ contacts formed by late transition metals to be nonlinear. This nonlinearity might be an effect of semicoordination, which is expected when the sulfur LP, which is not in the continuation of the $R-S$ bond, is directed to the electrophilic metal sites. We further focused on the theoretical consideration of several rather simple but representative complexes (Fig. 7) using various real-space and orbital methods to obtain a theory-supported insight into the effects of the nucleophilicity of metal sites and the geometry of a contact on the electronic structure and CT contributions within the most abundant $R-S\cdots M$ moieties.

First, the complex of a relatively nucleophilic gold(I) center [CSD refcode: PAJDIP (Voß *et al.*, 2012)] with the most shortened (0.43 Å with respect to ΣR_{vdW} among other relevant Au^{I} complexes) and nearly linear (175.1°) intramolecular $R-S\cdots M$ contact was studied as a system, where a strong metal-involving ChB was expected. Surprisingly, a very similar complex of nucleophilic gold(I) (PAJDOV; Voß *et al.*, 2012), which differs from PAJDIP only by the nature of the heterocyclic ligand, exhibits a less linear (169.0°) and pronouncedly less shortened (0.17 Å with respect to ΣR_{vdW}) $R-S\cdots M$ contact. This discrepancy between PAJDIP and PAJDOV was also interesting to analyze in order to reveal the role of the R atom in a possible interplay between CT contributions.

Nonlinear intramolecular $R-S\cdots M$ contacts with a relatively nucleophilic platinum(II) center were studied using the cationic complex WOVJOG01 as the model. This structure exhibits a rather small $\angle(R-S\cdots M)$ of 161.6° and significant

Figure 7
3D (top panel) and schematic (bottom panel) representation of systems with $R-S\cdots M$ contacts (dashed lines) analyzed in the present study: structures EGAXAN, PAJDIP and PAJDOV, dication of the WOVJOG01 salt, and contact ionic pair from the CEWROM structure. The $S\cdots M$ distances are 3.120 Å (EGAXAN), 3.034 Å (PAJDIP), 3.293 Å (PAJDOV), 3.100 Å (WOVJOG01), 3.513 Å (CEWROM).
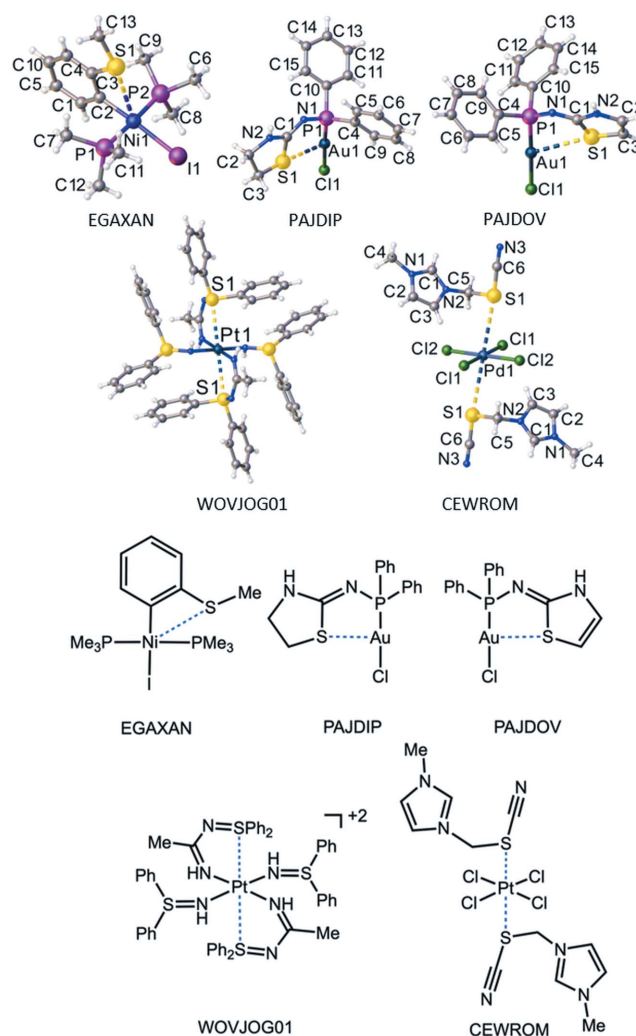

Figure 6
Heat plot of the shortening of the $S\cdots M$ distance with respect to appropriate ΣR_{vdW} (vertical axis, Å) versus $\angle(R-S\cdots M)$ (horizontal axis, °) in systems with intramolecular $R-S\cdots M$ contacts. The cell color denotes the distribution density.

Table 1
Selected geometric parameters of the model systems.

Refcode	Crystal			Gas (equilibrium)			
	$S \cdots M$ (Å)	$\angle(R-S \cdots M)$ (°)	$R-S$ (Å)	$S \cdots M$ (Å)	$\angle(R-S \cdots M)$ (°)	$R-S$ (Å)	Δ† (Å)
EGAXAN	3.120	169.2	1.801	3.107	169.1	1.806	0.11
PAJDIP	3.034	175.1	1.814	3.284	168.8	1.822	0.54
PAJDOV	3.293	169.0	1.747	3.419	154.1	1.742	1.03
WOVJOG01	3.100	161.6	1.796	3.139	156.7	1.800	0.44
CEWROM	3.513	175.8	1.699	3.719 *3.599*‡	157.8 *163.2*‡	1.700	0.39

† Δ is the weighted r.m.s. difference between crystal and gas structures overlapped by the best least-squares fit (no H atoms were considered). ‡ Parameters for the most shortened $C-S \cdots Cl$ contact are shown in italics; see also the text.

shortening (0.42 Å) compared with the other inspected Pt complexes with pronounced deviations ($< 165°$) of $\angle(R-S \cdots M)$ from 180°. The bonding situation in the WOVJOG01 structure was particularly challenging to analyze, as the $R-S \cdots M$ contact was overlooked for this structure in our previous study (Makarycheva-Mikhailova *et al.*, 2003).

According to our CSD processing, metals with a low nucleophilicity, such as nickel(II), also form relatively short intramolecular $R-S \cdots M$ contacts. The EGAXAN structure (Zhang *et al.*, 2014) is the most intriguing in this sense, as it is characterized by an approximately linear arrangement of R, S and M atoms (169.2°) and significant shortening (0.31 Å) of the $R-S \cdots M$ contact; this shortening is the largest among other relevant nickel(II) complexes. Although in EGAXAN, $\angle(R-S \cdots M)$ significantly deviates from 180° (by $> 10°$), it is still too large to unambiguously classify this contact as semi-coordination.

As indicated in Section 2.2.1, the distribution of the geometric parameters of intermolecular contacts (*i.e.* distances and angles) resembles intramolecular contacts, although the former are generally longer and exhibit smaller $\angle(R-S \cdots M)$. We assumed that the consideration of lengthened contacts potentially corresponding to weaker, more flexible interactions would provide structures with a more linear arrangement of R, S and M atoms corresponding to intermolecular ChB. For this purpose, the limited dataset of intermolecular contacts was extended to systems with an $S \cdots M$ distance less than $\Sigma R_{vdW} + 0.1$ Å. The structure of the palladium(II) salt CEWROM (Zhao *et al.*, 2007) was chosen for further theoretical studies, as it is characterized by the largest $\angle(R-S \cdots M)$ value (175.8°).

2.3. Theoretical calculations

2.3.1. General consideration of structures of the model complexes in the solid state and gas phase. According to the CSD processing, the geometry of an $R-S \cdots M$ interaction in crystals is potentially affected by concomitant intra- and intermolecular interactions. The response of structures of model complexes to the crystal–gas transition was studied by comparing the experimental crystal structures with isolated equilibrium structures obtained from the DFT calculations to independently confirm this hypothesis.

While essential structural features of all model complexes are similar in the crystal and isolated states, substantial differences were observed for $R-S \cdots M$ contacts in the Au and Pd complexes (Table 1 and Fig. 8). The intramolecular contacts in the gold(I) complexes PAJDIP and PAJDOV are significantly affected by the crystal environment. The $S \cdots Au$ distances increase (by > 0.1 Å) during the crystal-to-gas transition and are accompanied by a pronounced decrease in the corresponding $\angle(C-S \cdots Au)$ (by 6 and 15° for PAJDIP and PAJDOV, respectively). In PAJDIP, we probed the stability of corresponding geometries by performing a relaxed scan calculation of the potential energy surface along the coordinate of the $P-N-C-S$ torsion angle rotation, and no other energy minima were observed (barrier height ~ 10.1 kcal mol^{-1}). Thus, the favorable nonlinear arrangement of C, S and Au atoms (expected from the statistical analysis) is confirmed in the isolated complexes, where the geometric preferences of the $R-S \cdots M$ contact are unaffected by crystal packing forces. The differences in the $R-S \cdots M$ contacts and the rigidity of PAJDIP and PAJDOV (see the Δ parameter in Table 1) reveal effects of the R atom on the specifics of the $R-S \cdots M$ interaction, which will be further discussed in detail based on the analysis of the electronic structure (Section 2.3.3).

The ionic pair from the CEWROM structure also exhibited structural flexibility, which is manifested as an increase in the cation–anion separation accompanied by a shift of cations along the $PdCl_4^{2-}$ plane. Although the Pd, S and C atoms possess a nearly linear arrangement in the CEWROM crystal, the Cl atoms of the anionic moiety, rather than the Pd atom, shift closer to the CS fragment in the gas phase. The distributions of $S \cdots Cl/S \cdots Pd$ distances and $\angle(C-S \cdots Cl)/\angle(C-S \cdots Pd)$ in the isolated ionic pair of CEWROM resemble the

EGAXAN   PAJDIP   PAJDOV

WOVJOG01   CEWROM
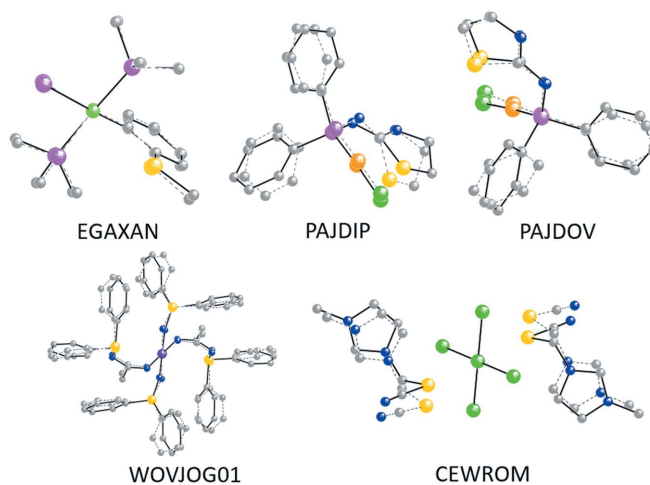
Figure 8
The best least-squares overlap of the crystal (solid lines) and isolated optimized (dashed lines) structures of complexes analyzed in the present study. For CEWROM, the best overlap of $PdCl_4^{2-}$ moieties is shown for clarity.

bifurcated metal-involving XBs (Ivanov *et al.*, 2016). The comparison of crystal and gas phase geometries for CEWROM explicitly indicates the insignificance of possible intermolecular $R{-}S{\cdots}M$ interactions, which is completely consistent with the limited CSD statistics for these structures (Section 2.2).

The differences between gas and crystal phase geometries of the WOVJOG01 and CEWROM structures are comparable (see the Δ parameter in Table 1), particularly if one takes into account a larger number of atoms in WOVJOG01. The parameters of the $C{-}S{\cdots}Pt$ contacts in WOVJOG01 are conserved, similar to the corresponding parameters of the $C{-}S{\cdots}Ni$ contact in EGAXAN. Based on the geometric criteria, the rigidity of the $C{-}S{\cdots}Pt$ contact in WOVJOG01 is presumed to be caused by other intramolecular forces, particularly by $S{\cdots}\pi$ and $\pi{\cdots}\pi$ interactions.

Surprisingly, the $C{-}S{\cdots}Ni$ contact in EGAXAN becomes slightly shorter in the isolated state, preserving its approximately linear directionality. This shorter contact might indicate the presence of an attractive $C{-}S{\cdots}Ni$ interaction. However, this attraction contradicts the limited number of published Ni complexes with shortened $R{-}S{\cdots}M$ contacts and a relatively low nucleophilicity of a nickel(II) LP. Notably, the EGAXAN gas structure deviates only slightly from the crystal state (see the Δ parameter in Table 1) and represents the only studied example where the $R{-}S$ bond elongation, which could be a manifestation of the pronounced CT onto the $\sigma^*(C{-}S)$ orbital, is accompanied by the shortening of the $S{\cdots}M$ distance.

2.3.2. Bonding situation in the Ni complex (EGAXAN). Furthermore, we focused on analyzing the real-space and orbital descriptors of interatomic interactions in the optimized isolated systems to validate the attractive character of $R{-}S{\cdots}M$ contacts and to understand the role of these contacts in the stabilization of complexes. Due to the insignificant number of relevant nickel(II) structures and low nucleophilicity of these metal centers, knowledge of the bonding situation in EGAXAN was particularly interesting.

The topographic analysis of the electron density $\rho(\mathbf{r})$ revealed no bonding $S{\cdots}Ni$ interaction (Fig. 9). This result is also consistent with the analysis of the electronic virial field topography. However, the visualization of the $\rho(\mathbf{r})$ zero-flux surfaces displayed a sufficient proximity of interatomic surfaces corresponding to $Ni{-}C$, $C{-}C$, and $S{-}C$ interactions in the region where the $\rho(\mathbf{r})$ $(3, -1)$ CP of the $S{\cdots}Ni$ bonding interaction could be located. Thus, some rather small shifts of nuclei might lead to the reconstruction of the $\rho(\mathbf{r})$ defined atomic connectivity graph and the appearance of $(3, -1)$ CP in the $S{\cdots}Ni$ area (Ananyev *et al.*, 2016). This finding is also consistent with the map of the $\text{sign}(\lambda_2)\rho(\mathbf{r})$ function [$\text{sign}(\lambda_2)$ denotes the sign of intermediate eigenvalue of $\rho(\mathbf{r})$ Hessian] onto the reduced density gradient (RDG) isosurfaces (Fig. S4) (Johnson *et al.*, 2010); a small volume of lowered norm of $\rho(\mathbf{r})$ gradient with a rather pronounced region of electronic charge concentration was observed in the expected region.

According to the analysis of ELF and $\nabla^2\rho(\mathbf{r})$ fields, neither of these charge concentrations are directed on the metal atom

in the equilibrium (see Fig. S4). The $\rho(\mathbf{r})$ topography for EGAXAN structures with the SMe fragment rotated with respect to the phenyl plane (from $2°$ in the equilibrium structure to $53°$ with a $3°$ step) were also studied to determine the possible dependence of the atomic connectivity graph on the proximity of the Ni atom to sulfur LPs. Even significant rotation of the SMe fragment and corresponding LPs does not lead to an emanation of the desirable CP.

The absence of the $\rho(\mathbf{r})$ $(3, -1)$ CP corresponding to the $S{\cdots}Ni$ interaction was rationalized by analyzing the sources of the $\rho(\mathbf{r})$ function (Bader & Gatti, 1998) in the area of $S{\cdots}Ni$ interaction in the optimized structure. The integration of the source function over QTAIM atomic basins was performed using the position of electron density minimum along the $S{\cdots}Ni$ separation as the reference point. While the nickel and iodine atoms contribute up to 50% of the charge (0.005 and 0.006 a.u., respectively) to the reference point (0.022 a.u.), the integral of the source function over the sulfur basin is negligibly small ($<1 \times 10^{-4}$ a.u.). The absence of $S{\cdots}Ni$ CP is presumed to be caused by this large inequality of contributions from Ni and S basins. We also did not find a $Se{\cdots}Ni$ $(3, -1)$ CP in the optimized model structure when the S atom was replaced with Se. The identity of the metal atom still remains as an important factor.

Commonly, the $\rho(\mathbf{r})$ $(3, -1)$ CP is believed to be an indicator of the preferred exchange interaction channel between atoms (Pendás *et al.*, 2007). Therefore, the total energy decomposition was analyzed with the Interacting Quantum Atoms (IQA) approach to determine the presence of attractive interactions between Ni and S topological atomic basins, as defined by QTAIM space partitioning. Indeed, the energy contribution from the $S{\cdots}Ni$ interaction is slightly negative
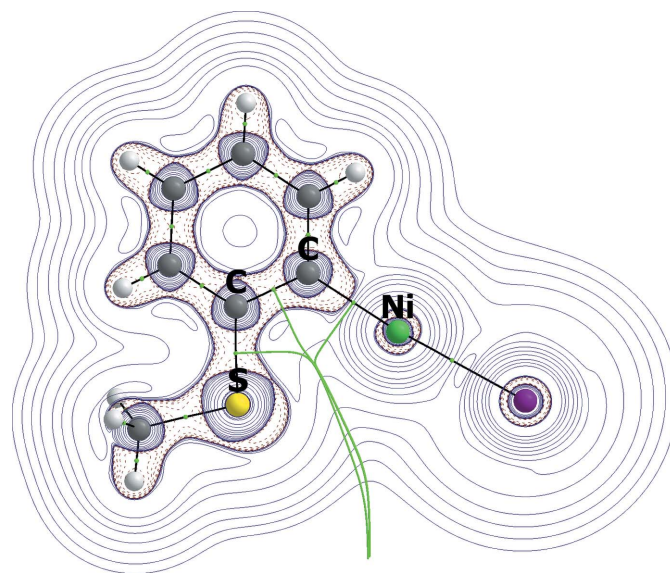
Figure 9
The $\nabla^2\rho(\mathbf{r})$ contour plot in the mean-squared $S{-}C{-}C{-}Ni$ plane of the isolated equilibrium EGAXAN structure (negative values are indicated by red dashed lines). The green dots denote $(3, -1)$ of $\rho(\mathbf{r})$. The green tubular lines correspond to three eigenvalue paths of selected interatomic surfaces.

Ananyev *et al.* • Structure-directing $S{\cdots}M$ noncovalent semicoordination bonding

(-8.3 kcal mol^{-1}) and only three times larger than the P—Ni contributions (-22.5 and -24.0 kcal mol^{-1}). For the S$\cdots$Ni interaction, the positive Coulomb potential energy contribution is overruled by the larger exchange-correlation energy (1.2 versus -9.5 kcal mol^{-1}). Although the energy contributions arising from an interaction between two topological atoms should not be directly compared with the energy of the chemical interaction, these contributions reveal an important role for a chemically meaningful exchange interaction between S and Ni atoms in the stabilization of the EGAXAN structure. Similar 'bond-path free' interactions with pronounced negative IQA interatomic contributions were reported in a previous study (Bartashevich, Pendás *et al.*, 2014).

As the IQA interatomic exchange-correlation energy may be identified with an emanation of covalent bonding (Menéndez-Crespo *et al.*, 2018), the conventional orbital descriptors were then analyzed within the NBO framework. The application of the second-order perturbation theory to NBOs revealed that the S$\cdots$Ni interaction can be regarded as the superposition of LP(S)$\rightarrow p$(Ni) and d(Ni)$\rightarrow\sigma^*$(C—S) CTs. While the latter is understood as the manifestation of metal-involved ChB, its energy (-0.6 kcal mol^{-1}) is significantly smaller than the former corresponding to a weak coordination bond (-8.9 kcal mol^{-1}).

Based on our calculations, the R—S$\cdots$Ni interactions should be more likely treated as coordination bonds rather than ChB, even at high values of $\angle(R$—S$\cdots$Ni). Consistent with the HSAB approach, these coordination bonds are too weak due to their small exchange contribution that is insufficient to localize these interactions upon an inspection of the electron density maps.

2.3.3. Bonding in the Au complexes (PAJDIP and PAJDOV). Although both gold(I) complexes are more sensitive to the crystal packing effects and exhibit less directionality of the R—S$\cdots M$ contact (Section 2.3.1), they are characterized by the presence of the corresponding topological indicators of the R—S$\cdots$Au bond (Fig. 10). As expected, the interaction in both systems is the closed-shell type [at the corresponding $\rho(\mathbf{r})$ CP $\nabla^2\rho(\mathbf{r}) > 0$, $h_e(\mathbf{r}) > 0$] with a low charge concentration between atomic basins [$\rho(\mathbf{r})$ values at the CP are 0.013 a.u. and 0.016 a.u. in PAJDOV and PAJDIP, respectively]. At the same time, these interactions are rather strong, as revealed by the estimations of contributions to the energy of the system based on properties of topological descriptors (-2.1, -1.9, -2.7 and -2.7, -2.5, -3.7 kcal mol^{-1} from the virial at CP (Espinosa *et al.*, 1998), kinetic energy density (Vener *et al.*, 2012) at CP and $\rho(\mathbf{r})$ surface integral (Romanova *et al.*, 2018), respectively, for PAJDOV and PAJDIP). The atomic connectivity graph in the area of R—S$\cdots$Au interaction was structurally stable (the corresponding $\rho(\mathbf{r})$ ellipticity values are 0.45 and 0.25 in PAJDOV and PAJDIP, respectively). This finding is consistent with the data obtained from the RDG isosurface analysis in this region, which revealed a volume of the lowered gradient norm that was larger than in EGAXAN and displayed a significant electronic charge concentration (Fig. S5). For comparison, the $\rho(\mathbf{r})$ function in the area of another stronger

(from -3.0 to -4.2 kcal mol^{-1}) closed-shell noncovalent interaction observed in both Au complexes, namely, the intramolecular CH$\cdots$N HB, is significantly flatter [$\rho(\mathbf{r})$ ellipticity are 6.9 and 4.4 for PAJDOV and PAJDIP, respectively] and displays a smaller charge concentration (Fig. S5).

Although the ELF maximums corresponding to sulfur LPs (Fig. S5) are again not directed toward the metal atom, the bond path between S and Au nuclei passes through the concentration of electronic charge on the sulfur atom (Fig. 9). The hypothesis that the sulfur atom functions as a nucleophile is supported by the NBO analysis. The ChB-like d(Au)$\rightarrow\sigma^*$(C—S) CT stabilizes the complexes only slightly
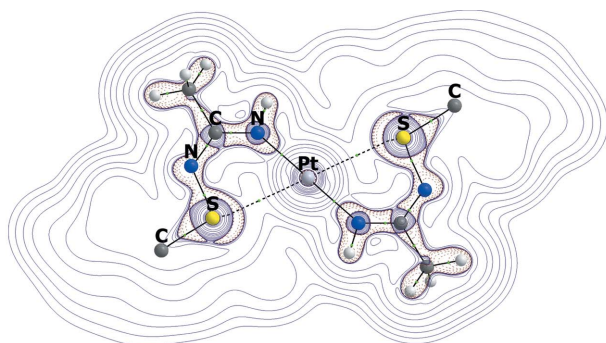

(a)

(b)
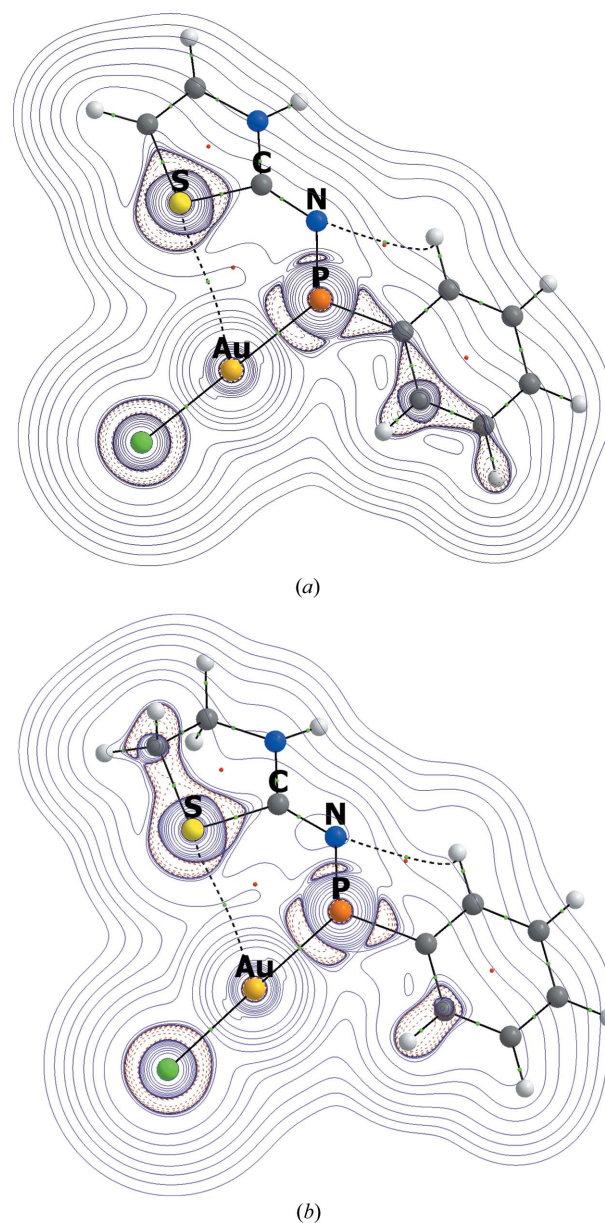
Figure 10
The $\nabla^2\rho(\mathbf{r})$ contour plot of the mean-squared S—C—C—Au plane of the isolated equilibrium PAJDOV (top) and PAJDIP (bottom) structures (negative values are given by red dashed lines). The green dots and red dots denote (3, -1) and (3, $+1$) CPs of $\rho(\mathbf{r})$, respectively, while the bold dashed lines correspond to bond paths of noncovalent interactions.

(-0.5 and -1.6 kcal mol^{-1} in PAJDOV and PAJDIP, respectively), whereas the contributions of LPs(S)$\rightarrow p$(Au) and LPs(S)$\rightarrow s$(Au) CTs are several times larger (-7.5 and -9.6 kcal mol^{-1} in PAJDOV and PAJDIP, respectively). The corresponding description of the $R-$S$\cdots$Au interactions in PAJDOV and PAJDIP predominantly as semicoordination bonds (weak coordination bonds with significant charge depletion between the atoms) is consistent with the decrease of $\angle(R-$S$\cdots$Au) upon the crystal-to-gas transition.

The greater strength and topological stability of the $R-$S$\cdots$Au interaction in PAJDIP are consistent with the relative rigidity of this structure (Table 1 and the discussion in Section 2.3.1). The difference between PAJDOV and PAJDIP is potentially rationalized by the difference in the inductive effect on the sulfur atom, which is formally larger in PAJDIP containing a Csp^3 atom at the R substituent. This conclusion agrees well with the differences in LPs(S)$\rightarrow$Au CTs explored using the NBO analysis. The strengthening of the $R-$S$\cdots$Au interactions upon an increase in the electron-donor properties of RS fragment serves as an additional indication of the semicoordination character of the $R-$S$\cdots$Au interactions.

2.3.4. Bonding in the Pt complex (WOVJOG01). The Pt coordination polyhedron is also supported by the presence of two bonding $R-$S$\cdots$Pt interactions, as revealed by the QTAIM analysis (Fig. 11). These interactions are of the intermediate type [at the corresponding $\rho(\mathbf{r})$ CP $\nabla^2\rho(\mathbf{r}) > 0$, $h_e(\mathbf{r}) < 0$], while their energy contributions are lower than corresponding values in the Au complexes (for each interaction, -4.3, -3.6 and -5.3 kcal mol^{-1} from the virial at CP (Espinosa *et al.*, 1998), kinetic energy density (Vener *et al.*, 2012) at CP and $\rho(\mathbf{r})$ surface integral (Romanova *et al.*, 2018), respectively). Although this interaction can be regarded as noncovalent due to its low absolute values of $\nabla^2\rho(\mathbf{r})$ and $h_e(\mathbf{r})$ compared with conventional covalent bonds, its relatively large strength is consistent with the analysis of charge concentrations, which showed the CT channels of coordination bond in the area under study. The ELF isosurface corresponding to the sulfur LP is directed toward the metal atom (Fig. S6), while the $R-$S$\cdots$Pt bond paths pass through electron density concentrations on sulfur atoms (Fig. 11). The NBO analysis also shows considerable contributions from LP(S)$\rightarrow p$(Pt) and LP(S)$\rightarrow s$(Pt) CTs to the total energy of a system (-24.7 kcal mol^{-1}). Again, the opposite ChB-like d(Pt)$\rightarrow \sigma^*$(C$-$S) CT contribution is significantly smaller (-2.6 kcal mol^{-1}), but somewhat more pronounced than in the Au and Ni complexes. The discussed parameters of the $R-$S$\cdots$Pt interaction confirm our statistical observations of large fractions of relevant $5d$ metal complexes with the nonlinear arrangement of R, S and M atoms (see Section 2.2).

As indicated above (Section 2.1.1), the differentiation between coordination and semicoordination bonds based on the weights of the $\rho(\mathbf{r})$-based atomic connectivity graph is controversial, as the total electronic energy density $h_e(\mathbf{r})$ that was analyzed to typify the topological bonding strongly depends on approximations obtained using a particular theoretical method. Moreover, the differentiation between types of topological bonding (namely, shared interactions, intermediate and closed-shell types of interactions) is only qualitative and should not be used for a quantitative estimate of the covalent and ionic contributions. Although the $R-$S$\cdots$Pt interactions in WOVJOG01 are characterized by a pronounced covalent character [$h_e(\mathbf{r}) < 0$], the conventional paradigm prevents the consideration of these interactions as coordination bonds in the platinum(II) complex. For instance, the Pt$-$N coordination bonds in this complex are characterized by significantly lower $h_e(\mathbf{r})$ values (-0.05 a.u. versus -4×10^{-4} a.u. for $R-$S$\cdots$Pt) and a considerably larger strength [for two symmetrically independent bonds, $-66.0/-65.5$, $-42.7/-41.9$ and $-36.4/-36.6$ kcal mol^{-1} from the virial at CP (Espinosa *et al.*, 1998) kinetic energy density (Vener *et al.*, 2012) at CP and $\rho(\mathbf{r})$ surface integral, respectively (Romanova *et al.*, 2018)]. The estimate of coordination bond energies from the weights of QTAIM atomic connectivity graph were already shown to provide reasonable results for bonds formed by $3d$ or $5d$ metals and neutral or even charged ligands (Borissova *et al.*, 2008; Ananyev *et al.*, 2013). Based on the data for Pt bonds in WOVJOG01, the $R-$S$\cdots$Pt interaction is suggested to be a weak noncovalent coordination bond or semicoordination bond.

This consideration is consistent with similar energetics of other intramolecular noncovalent interactions observed using the QTAIM analysis (Fig. S7, in total, -17.6 to -21.0 kcal mol^{-1} versus -7.2 to -10.6 kcal mol^{-1} for two $R-$S$\cdots$Pt interactions). Thus, a number of bonding closed-shell diatomic interactions within each pair of ligands was observed in WOVJOG01, including interactions corresponding to the π–π stacking interactions between the phenyl rings. Overall, the sum of the noncovalent interactions provides a considerable contribution to the stability of the system (from -24.8 to -31.6 kcal mol^{-1}), which is comparable to Pt$-$N coordination bonds. This finding is consistent with the conservative conformation of this complex (Section 2.3.1).

According to our calculations, the $R-$S$\cdots$Pt interactions in WOVJOG01 correspond to semicoordination bonding. Despite their relatively small energy, the $R-$S$\cdots$Pt semicoordination bonds support the square-planar polyhedron,

Figure 11
The $\nabla^2\rho(\mathbf{r})$ contour plot of the mean-squared S$-$N$-$C$-$N$-$Pt plane of the isolated equilibrium WOVJOG01 structure (negative values are given by red dashed lines). The green dots denote (3, -1) CPs of $\rho(\mathbf{r})$, while the bold dashed curves correspond to bond paths of the $R-$S$\cdots$Pt interactions.

Ananyev *et al.* · Structure-directing S$\cdots M$ noncovalent semicoordination bonding

forming the quasi-octahedron with four coordination and two semicoordination bonds of the charge-depleted platinum(II) in the cationic complex.

2.3.5. Bonding in the ionic pair of Pd complex (CEWROM). As expected from the structural data (Section 2.3.1), the ionic pair isolated from the CEWROM crystal structure changes its noncovalent bonding network during the crystal-to-gas transition (Fig. 12). While three $C-H\cdots Cl$ hydrogen bonds between the counterions are present in both the equilibrium and crystal geometries, the connectivity of the sulfur atom differs. We observed two topological interactions with Pd and Cl atoms in equilibrium and only one topological $R-S\cdots Pd$ bond in the crystal geometry. All noncovalent diatomic interactions are the closed-shell type [at the corresponding $\rho(\mathbf{r})$ CPs $\nabla^2\rho(\mathbf{r}) > 0$, $h_e(\mathbf{r}) > 0$]. Although the HBs are less covalent in these terms [*i.e.* larger $\nabla^2\rho(\mathbf{r})$ and $h_e(\mathbf{r})$ values], the changes in their energy contributions are meaningless. According to different schemes, the HBs are only slightly less favorable in the equilibrium structure [-4.7, -5.1, and -5.4 versus -4.8, -5.2, and -5.5 kcal mol^{-1} in the crystal geometry from, respectively, the virial at CP (Espinosa *et al.*, 1998), kinetic energy density (Vener *et al.*, 2012) at CP and $\rho(\mathbf{r})$ surface integral (Romanova *et al.*, 2018)]. As expected from the changes in the atomic connectivity graph, the noncovalent bonding of sulfur atom provides more stabilizing contributions in the equilibrium structure [-1.7, -2.0, and -2.7 versus -1.2, -1.3, and -1.8 kcal mol^{-1} in the crystal geometry from, respectively, virial at CP (Espinosa *et al.*, 1998), kinetic energy density (Vener *et al.*, 2012) at CP and $\rho(\mathbf{r})$ surface integral

(Romanova *et al.*, 2018)]. Thus, the changes in topological bonding that occurred in the $R-S\cdots(Pd-Cl)$ fragment may provide a significant contribution to the overall stabilization of the system during the crystal-to-gas transition (the total energy change is 5.0 kcal mol^{-1}).

For the equilibrium geometry, the thorough analysis of the region between Pd, S and Cl atoms suggests that the $R-S\cdots Pd$ and $R-S\cdots Cl$ bond paths are the manifestation of a more general bifurcate interaction. Indeed, two corresponding $(3, -13, -1)$ CPs of $\rho(\mathbf{r})$ are characterized by similar values of weights, such as $\rho(\mathbf{r})$, λ_2, $\nabla^2\rho(\mathbf{r})$ and ellipticity values (respectively, 0.006, -0.002, 0.020 a.u. and 0.234 for $R-S\cdots Cl$ and 0.006, -0.001, 0.017 a.u. and 0.332 for $R-S\cdots Pd$). The energy values of both topological interactions are also similar and differ by less than 0.1 kcal mol^{-1}. This finding, together with the analysis of the sign$(\lambda_2)\rho(\mathbf{r})$ function mapped onto the RDG isosurface (Fig. S8), confirms the flatness of electron distribution in the $R-S\cdots(Pd-Cl)$ bonding area. Moreover, the $\nabla^2\rho(\mathbf{r})$ 2D maps in the Pd$-$Cl$-$S, C$-$S$-$Cl and C$-$S$-$Pd planes (Fig. 13 and Fig. S9) are nearly identical and show that both bond paths pass through electron charge concentrations on the S atom that are similar in magnitude.

A different bonding situation is observed for the crystal geometry, where the specific features of electron density distribution in the area of $R-S\cdots Pd$ interaction reveal its rather large directionality [the ellipticity value at the corresponding CP is 0.09, see also sign$(\lambda_2)\rho(\mathbf{r})$ maps in Fig. S10].

(*a*)

(*b*)
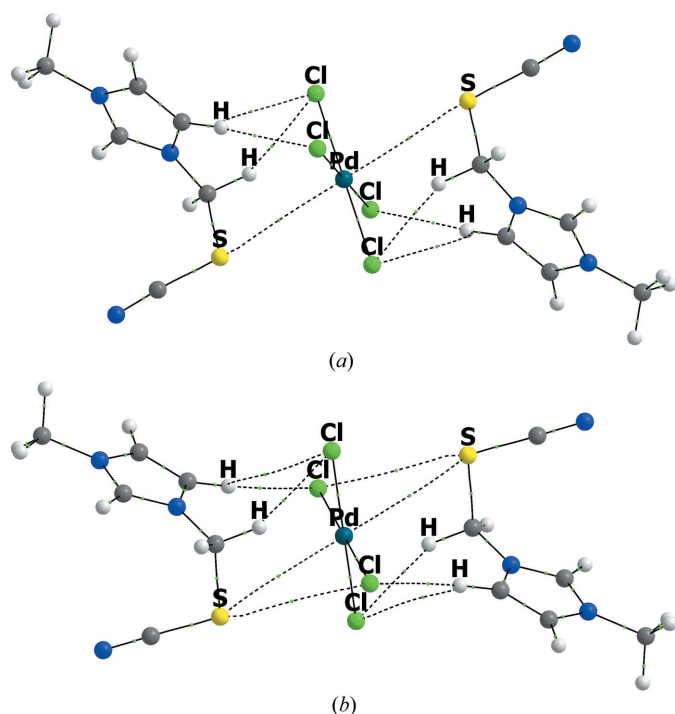
Figure 12
The full atomic connectivity graphs of the isolated ionic pair from the CEWROM structure with the crystal (top) and equilibrium (bottom) geometries. The green dots denote $(3, -1)$ CPs of $\rho(\mathbf{r})$. Bond paths of noncovalent interactions are shown by dashed lines.
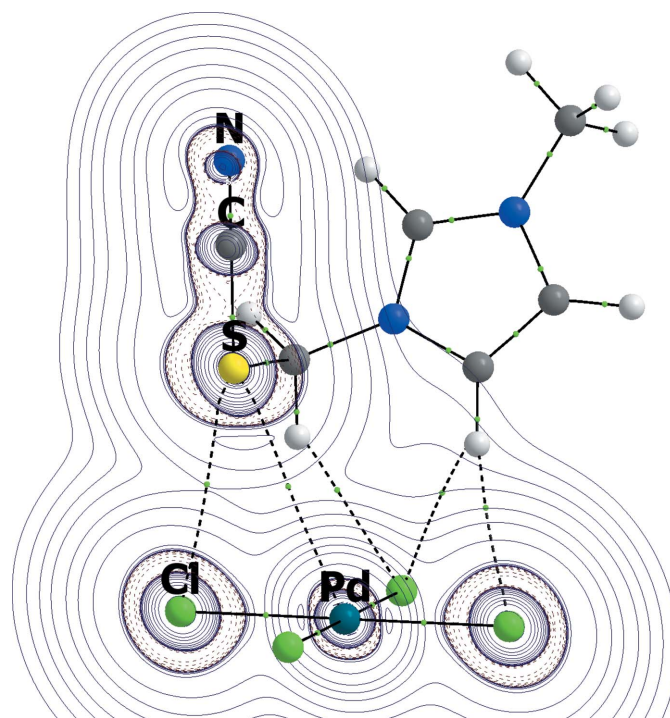
Figure 13
The $\nabla^2\rho(\mathbf{r})$ contour plot in the Pd$-$Cl$-$S plane of the fragment of the isolated equilibrium CEWROM ionic pair (negative values are given by red dashed lines). The green dots denote $(3, -1)$ CPs of $\rho(\mathbf{r})$, while the bold dashed lines correspond to bond paths of bonding noncovalent interactions.

This result is consistent with the large value of the $\angle(R-$S$\cdots$Pd$)$ in the crystal (Table 1) and $\nabla^2\rho(\mathbf{r})$ maps (Fig. 14), indicating a sufficient compression of electron charge concentration on the sulfur atom in the area of corresponding bond path. This compression is potentially regarded as the manifestation of a more pronounced ChB-like CT.

However, in both geometries, the contribution of ChB-like CT is negligible compared with contribution from LP(S)$\rightarrow p$(Pd) and LP(S)$\rightarrow s$(Pd) CTs (-1.2 and -0.5 kcal mol^{-1} versus -9.9 and -7.6 kcal mol^{-1} in the crystal and equilibrium geometries, respectively), but the d(Pd)$\rightarrow\sigma^*$(C$-$S) CT is more favorable in the crystal geometry. In the equilibrium structure, we also observed small LP(Cl)$\rightarrow\sigma^*$(C$-$S) and LP(S)$\rightarrow\sigma^*$(Pd$-$Cl) CTs (both 0.7 kcal mol^{-1}).

Based on our analysis, the semicoordination bonding is the preferred configuration of $R-$S$\cdots M$ interactions, even if the anionic metal-containing species is used and a large $\angle(R-$S$\cdots M)$ (175.8° for the crystal geometry of CEWROM) is observed.

3. Concluding remarks

The short $R-$S$\cdots M$ contacts in the late transition metal complexes of different types are potentially attributed to semicoordination bonding rather than metal-involving chalcogen bonding. Indeed, the analysis of CT contributions and electron density distribution revealed that the $R-$S$\cdots M$ interactions exhibit only a small ChB character. The predominant coordination bond character of $R-$S$\cdots M$ interactions is consistent with the tendency of these interactions to be stronger upon increases in the nucleophilicity of a sulfur center and the electrophilicity of the corresponding metal

center. Accordingly, the strongest interaction is observed for the cationic platinum(II) complex (CSD refcode: WOVJOG01; see Fig. 7 and Section 2.3.4) with the pronounced electrophilicity of the Pt^{II} center caused by the positive charge on the cation. In turn, the $R-$S$\cdots M$ interaction becomes weaker if R is a poor electron donor and the metal is less electrophilic, based on our calculations of the gold(I) complexes (CSD refcodes: PAJDIP and PAJDOV). The limiting case under concern is the EGAXAN complex (see Figs. 7 and 9, and Section 2.3.2), where the electron-donor environment does not provide sufficient electrophilicity of the nickel(II) center for the bonding $R-$S$\cdots$Ni interaction, although a non-negligible exchange-correlation interaction contribution was detected within the IQA framework. The absence of the $R-$S$\cdots$Ni coordination bond in EGAXAN is consistent with a larger contribution into electron distribution between S and Ni arising from the metal. The presence of the electron-donor sulfur atom in EGAXAN provides a smaller electron contribution than the metal center and it contradicts the general approach to coordination bonding.

The NBO analysis supports the hypothesis that $R-$S$\cdots M$ interactions represent semicoordination bonding by showing a significant increase in LP(S)$\rightarrow M$ CT (up to 24.7 kcal mol^{-1}) upon strengthening of the $R-$S$\cdots M$ interaction. However, this hypothesis is also verified for the opposite d(M)$\rightarrow\sigma^*$(C$-$S) CT, which is slightly larger in complexes with stronger $R-$S$\cdots M$ interactions, although still remaining small in value (<2.7 kcal mol^{-1}). According to the NBO analysis, the largest energy contribution corresponding to this type of CT is observed for the gold(I) and platinum(II) complexes (CSD refcodes: PAJDIP and WOVJOG01, respectively). Among other studied systems, these two complexes are formally considered as complexes with the most pronounced nucleophilic regions on a metal center, if the charge of a complex and donor abilities of ligands are not considered. We anticipate that the combination of a proper metal with a particular nucleophilicity and a more σh-donating RCh fragment, such as RSe and RTe, will result in a sufficient increase in the d(M)$\rightarrow\sigma^*$(C$-$S) CT and the formation of metal-involving ChBs. A comparison of the strength and directionality of these interactions with weak $R-$S$\cdots M$ semicoordination bonds would be particularly interesting.

Nonetheless, although the $R-$S$\cdots M$ interactions are too weak to be the only structure-directing force of supramolecular aggregation (from -1.2 to -5.3 kcal mol^{-1} according to different estimation schemes) and are easily affected by other noncovalent interactions, they still determine structural features of complexes, and this effect is particularly noticeable for intramolecular interactions. Consistent with the CSD statistics, our theoretical analyses of the formal crystal-to-gas transitions reveal that the architecture of these intramolecular interactions favors the nonlinear arrangement of R, S and M atoms. Moreover, according to the potential energy scan of the EGAXAN and PAJDIP structures, the $R-$S$\cdots M$ interaction represents an important factor stabilizing a particular conformation of the whole metal complex.
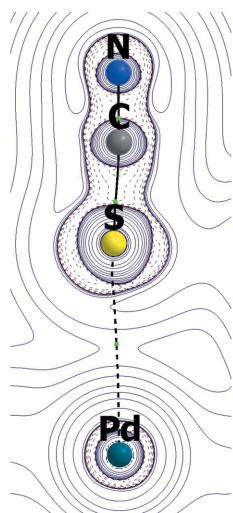

Figure 14
The $\nabla^2\rho(\mathbf{r})$ contour plot of the Pd$-$Cl$-$S plane of the fragment of the isolated CEWROM ionic pair at crystal geometry (negative values are given by red dashed lines). The green dots denote (3, -1) CPs of $\rho(\mathbf{r})$, while the bold dashed lines correspond to bond paths of bonding noncovalent interactions.

research papers

4. Computational details and data processing

The CSD analysis was performed using the statistical suite of the CSD software (version CSD 2019) (Macrae *et al.*, 2020). The CSD search was constrained to the well defined (*R*1 < 5%) non-polymeric single-crystal structures possessing no errors and no formal disorder.

All quantum chemistry calculations, including those for the space and electronic structure analyses, were performed in the *Gaussian09* program (Frisch *et al.*, 2016) (revision D.01) within the DFT framework [the PBE0 hybrid functional (Perdew *et al.*, 1996; Adamo & Barone, 1999)]. The Grimme D3 corrections with Becke–Johnson damping were employed to accurately describe dispersion interactions (Grimme *et al.*, 2011). Full geometry optimization procedures were carried out starting from crystal geometries for all systems with standard converging criteria. The Hessian of total electronic energy was calculated for each system to confirm the type of saddle point: all optimized structures correspond to energy minima. The relaxed scan calculations for the PAJDIP structure was done with the P—N—C—S torsion angle being rotated on 180° (ten steps of 18°). The CEWROM ionic pair was also studied at the crystal geometry with the partial optimization of hydrogen atom positions. Nuclear coordinates of all studied structures are given in supporting information (Tables S1–S5).

The optimization, Hessian and relaxed scan calculations were done by using all-electron aug-cc-pVTZ basis sets for light atoms (up to Ni) (Dunning, 1989; Woon & Dunning, 1993). Heavy atoms were treated with the help of energy-consistent fully relativistic core pseudopotentials by the Stuttgart group combined with cc-pVTZ basis sets for valence electrons (Peterson *et al.*, 2007; Figgen *et al.*, 2005; Peterson *et al.*, 2006; Figgen *et al.*, 2009). Iodine, palladium, platinum and gold atoms had 28, 28, 60 and 60 inner electrons, respectively, described by pseudopotentials.

The electronic structure analyses were based on single-point Douglas–Kroll–Hess (Reiher, 2006) fourth-order relativistic calculations including spin-orbit terms with x2c-TZVPPall basis sets (Pollak & Weigend, 2017). The calculations of ELF, RDG and sign(λ_2)$\rho(\mathbf{r})$ functions were performed using the *MultiWFN* program (Lu & Chen, 2012). The QTAIM studies [electron density/virial topographical analyses and integrations over $\rho(\mathbf{r})$ zero-flux surfaces] were performed in the *AIMAll* program (Keith, 2019). For the EGAXAN structure, the critical point search was additionally performed within a sphere of 3.0 Å radius, which were centered in the middle of the Ni···S separation and contained 100 000 grid points. Estimations of charge transfer contributions were performed in the *NBO3.1* program (Glendening *et al.*, 2003). Some theoretical descriptors of *R*—S···*M* interactions in the studied complexes are summarized in Table S6.

The IQA analysis for EGAXAN was performed using explicit calculations of exchange-correlation energy and other terms according to the scheme implemented in *AIMAll* for the PBE0 functional. For IQA, the single point calculation of the equilibrium EGAXAN structure was additionally performed using the 6-311G** basis set for the iodine atom and aug-cc-pVTZ for other atoms. Note that the DFT energy decomposition scheme used for IQA atomic contributions is approximate.

References

Aakeroy, C. B., Bryce, D. L., Desiraju, G. R., Frontera, A., Legon, A. C., Nicotra, F., Rissanen, K., Scheiner, S., Terraneo, G., Metrangolo, P. & Resnati, G. (2019). *Pure Appl. Chem.* **91**, 1889–1892.

Adamo, C. & Barone, V. (1999). *J. Chem. Phys.* **110**, 6158–6170.

Alkorta, I., Elguero, J. & Frontera, A. (2020). *Crystals*, **10**, 180.

Alkorta, I., Rozas, I. & Elguero, J. (1998). *Struct. Chem.* **9**, 243–247.

Ananyev, I. V., Karnoukhova, V. A., Dmitrienko, A. O. & Lyssenko, K. A. (2017). *J. Phys. Chem. A*, **121**, 4517–4522.

Ananyev, I. V. & Lyssenko, K. A. (2016). *Mendeleev Commun.* **26**, 338–340.

Ananyev, I. V., Medvedev, M. G., Aldoshin, S. M., Eremenko, I. L. & Lyssenko, K. A. (2016). *Russ. Chem. Bull.* **65**, 1473–1487.

Ananyev, I. V., Nefedov, S. E. & Lyssenko, K. A. (2013). *Eur. J. Inorg. Chem.* **2013**, 2736–2743.

Awwadi, F., Willett, R. D. & Twamley, B. (2011). *Cryst. Growth Des.* **11**, 5316–5323.

Bader, R. F. W. & Essén, H. (1984). *J. Chem. Phys.* **80**, 1943–1960.

Bader, R. F. W. & Gatti, C. (1998). *Chem. Phys. Lett.* **287**, 233–238.

Bartashevich, E. V., Matveychuk, Y. V., Troitskaya, E. A. & Tsirelson, V. G. (2014). *Comput. Theor. Chem.* **1037**, 53–62.

Bartashevich, E. V., Pendás, Á. M. & Tsirelson, V. G. (2014). *Phys. Chem. Chem. Phys.* **16**, 16780–16789.

Batsanov, S. S. (2001). *Inorg. Mater.* **37**, 871–885.

Benson, S. W. (1965). *J. Chem. Educ.* **42**, 502.

Bikbaeva, Z. M., Ivanov, D. M., Novikov, A. S., Ananyev, I. V., Bokach, N. A. & Kukushkin, V. Y. (2017). *Inorg. Chem.* **56**, 13562–13578.

Blanco, M. A., Martín Pendás, A. & Francisco, E. (2005). *J. Chem. Theory Comput.* **1**, 1096–1109.

Bondi, A. (1966). *J. Phys. Chem.* **70**, 3006–3007.

Borissova, A. O., Korlyukov, A. A., Antipin, M. Y. & Lyssenko, K. A. (2008). *J. Phys. Chem. A*, **112**, 11519–11522.

Brown, D. S., Lee, J. D., Melsom, B. G. A., Hathaway, B. J., Procter, I. M. & Tomlinson, A. A. G. (1967). *Chem. Commun.* pp. 369–371.

Carpenter, J. E. & Weinhold, F. (1988). *J. Mol. Struct. Theoret. Chem.* **169**, 41–62.

Cottrell, T. L. (1958). *The Strengths of Chemical Bonds*, 2d ed. London: Butterworth.

Cremer, D. & Kraka, E. A. (1984). *Croat. Chem. Acta*, **57**, 1259–1281.

Darwent, B. deB. (1970). *Nat. Stand. Ref. Data Ser. Nat. Bur. Stand.* **31**, 1–52.

Dunning, T. H. Jr (1989). *J. Chem. Phys.* **90**, 1007–1023.

Efimenko, Z. M., Novikov, A. S., Ivanov, D. M., Piskunov, A. V., Vereshchagin, A. A., Levin, O. V., Bokach, N. A. & Kukushkin, V. Y. (2020). *Inorg. Chem.* **59**, 2316–2327.

Espinosa, E., Molins, E. & Lecomte, C. (1998). *Chem. Phys. Lett.* **285**, 170–173.

Figgen, D., Peterson, K. A., Dolg, M. & Stoll, H. (2009). *J. Chem. Phys.* **130**, 164108.

Figgen, D., Rauhut, G., Dolg, M. & Stoll, H. (2005). *Chem. Phys.* **311**, 227–244.

Foster, J. P. & Weinhold, F. (1980). *J. Am. Chem. Soc.* **102**, 7211–7218.

Frisch, M. J. *et al.* (2016). *Gaussian09*. Revision D.01. Gaussian Inc., Wallingford CT, USA.

Glendening, E. D., Reed, A. E., Carpenter, J. E. & Weinhold, F. (2003). *NBO*, Version 3.1. Gaussian Inc., Pittsburgh, USA.

Grimme, S., Ehrlich, S. & Goerigk, L. (2011). *J. Comput. Chem.* **32**, 1456–1465.

Groom, C. R., Bruno, I. J., Lightfoot, M. P. & Ward, S. C. (2016). *Acta Cryst.* B**72**, 171–179.

Ho, Y., Cheng, E. C.-C., Tiekink, E. R. T. & Yam, V. W.-W. (2006). *Inorg. Chem.* **45**, 8165–8174.

Ivanov, D. M., Novikov, A. S., Ananyev, I. V., Kirina, Y. V. & Kukushkin, V. Y. (2016). *Chem. Commun.* **52**, 5565–5568.

Jeziorski, B., Moszynski, R. & Szalewicz, K. (1994). *Chem. Rev.* **94**, 1887–1930.

Johnson, E. R., Keinan, S., Mori-Sánchez, P., Contreras-García, J., Cohen, A. J. & Yang, W. (2010). *J. Am. Chem. Soc.* **132**, 6498–6506.

Keith, T. A. (2019). *AIMAll*, Version 16.05.18. TK Gristmill Software, Overland Park, KS, USA; http://aim.tkgristmill.com

Kerr, J. A. (1966). *Chem. Rev.* **66**, 465–500.

Lane, J. R., Hansen, A. S., Mackeprang, K. & Kjaergaard, H. G. (2017). *J. Phys. Chem. A*, **121**, 3452–3460.

Lu, T. & Chen, F. (2012). *J. Comput. Chem.* **33**, 580–592.

Lyssenko, K. A. (2012). *Mendeleev Commun.* **22**, 1–7.

Macrae, C. F., Sovago, I., Cottrell, S. J., Galek, P. T. A., McCabe, P., Pidcock, E., Platings, M., Shields, G. P., Stevens, J. S., Towler, M. & Wood, P. A. (2020). *J. Appl. Cryst.* **53**, 226–235.

Makarycheva-Mikhailova, A. V., Bokach, N. A., Kukushkin, V. Y., Kelly, P. F., Gilby, L. M., Kuznetsov, M. L., Holmes, K. E., Haukka, M., Parr, J., Stonehouse, J. M., Elsegood, M. R. J. & Pombeiro, A. J. L. (2003). *Inorg. Chem.* **42**, 301–311.

Matta, C. F. & Boyd, R. J. (2007). *The Quantum Theory of Atoms in Molecules: From Solid State to DNA, Drug Design.* Weinheim: Wiley-VCH Verlag.

Menéndez-Crespo, D., Costales, A., Francisco, E. & Martín Pendás, Á. (2018). *Chem. Eur. J.* **24**, 9101–9112.

Minkin, V. I. (1999). *Pure Appl. Chem.* **71**, 1919–1981.

Muller, P. (1994). *Pure Appl. Chem.* **66**, 1077–1184.

Nakane, D., Funahashi, Y., Ozawa, T. & Masuda, H. (2009). *Trans. Mater. Res. Soc. Jpn*, **34**, 513–516.

Nelyubina, Y. V., Korlyukov, A. A., Fedyanin, I. V. & Lyssenko, K. A. (2013). *Inorg. Chem.* **52**, 14355–14363.

Pearson, R. G. (1963). *J. Am. Chem. Soc.* **85**, 3533–3539.

Pendás, A. M., Francisco, E., Blanco, M. A. & Gatti, C. (2007). *Chem. Eur. J.* **13**, 9362–9371.

Perdew, J. P., Ernzerhof, M. & Burke, K. (1996). *J. Chem. Phys.* **105**, 9982–9985.

Peterson, K. A., Figgen, D., Dolg, M. & Stoll, H. (2007). *J. Chem. Phys.* **126**, 124101.

Peterson, K. A., Shepler, B. C., Figgen, D. & Stoll, H. (2006). *J. Phys. Chem. A*, **110**, 13877–13883.

Politzer, P., Murray, J. S., Clark, T. & Resnati, G. (2017). *Phys. Chem. Chem. Phys.* **19**, 32166–32178.

Pollak, P. & Weigend, F. (2017). *J. Chem. Theory Comput.* **13**, 3696–3705.

Popelier, P. (2016). *The Chemical Bond – 100 years old and Getting Stronger*, edited by M. Mingos, pp. 71–117. Switzerland: Springer.

Reed, A. E., Curtiss, L. A. & Weinhold, F. (1988). *Chem. Rev.* **88**, 899–926.

Reed, A. E. & Weinhold, F. (1983). *J. Chem. Phys.* **78**, 4066–4073.

Reed, A. E., Weinstock, R. B. & Weinhold, F. (1985). *J. Chem. Phys.* **83**, 735–746.

Reiher, M. (2006). *Theor. Chem. Acc.* **116**, 241–252.

Romanova, A., Lyssenko, K. & Ananyev, I. (2018). *J. Comput. Chem.* **39**, 1607–1616.

Saleh, G., Gatti, C. & Lo Presti, L. (2015). *Comput. Theor. Chem.* **1053**, 53–59.

Santra, B. K., Reddy, P. A. N., Nethaji, M. & Chakravarty, A. R. (2002). *Inorg. Chem.* **41**, 1328–1332.

Scheiner, S., Michalczyk, M. & Zierkiewicz, W. (2020). *Coord. Chem. Rev.* **405**, 213136.

Scilabra, P., Terraneo, G. & Resnati, G. (2019). *Acc. Chem. Res.* **52**, 1313–1324.

Shaik, S., Danovich, D., Braida, B., Wu, W. & Hiberty, P. C. (2015). *The Chemical Bond – 100 years old and getting stronger. Struct. Bond.* pp. 169–211. Springer Nature.

Silva Lopez, C. & R. de Lera, A. (2011). *Curr. Org. Chem.* **15**, 3576–3593.

Starodub, V. A., Vitushkina, S. V., Kamenskyi, D., Anders, A. G., Cheranovskii, V. O., Schmidt, H., Steinborn, D., Potočňák, I., Kajňaková, M., Radváková, A. & Feher, A. (2012). *J. Phys. Chem. Solids*, **73**, 350–356.

Tomlinson, A. A. G., Hathaway, B. J., Billing, D. E. & Nichols, P. (1969). *J. Chem. Soc. A*, pp. 65–71.

Valach, F. (1999). *Polyhedron*, **18**, 699–706.

Valach, F., Rohlíček, J., Lukeš, V., Kožíšek, J. & Jorík, V. (2018). *Inorg. Chim. Acta*, **479**, 106–112.

Vener, M. V., Egorova, A. N., Churakov, A. V. & Tsirelson, V. G. (2012). *J. Comput. Chem.* **33**, 2303–2309.

Vogel, L., Wonner, P. & Huber, S. M. (2019). *Angew. Chem. Int. Ed.* **58**, 1880–1891.

Voß, C., Pattacini, R. & Braunstein, P. (2012). *C. R. Chim.* **15**, 229–236.

Wikaira, J. L., Bruda, S., Landee, C. P. & Turnbull, M. M. (2017). *J. Coord. Chem.* **70**, 3880–3891.

Woon, D. E. & Dunning, T. H. Jr (1993). *J. Chem. Phys.* **98**, 1358–1371.

Xie, Y.-B., Zhang, C., Li, J.-R. & Bu, X.-H. (2004). *Dalton Trans.* pp. 562–569.

Zhang, W., Li, X. & Sun, H. (2014). *Inorg. Chim. Acta*, **419**, 7–10.

Zhao, D., Fei, Z., Han Ang, W., Scopelliti, R. & Dyson, P. J. (2007). *Eur. J. Inorg. Chem.* **2007**, 279–284.

Ananyev *et al.* · Structure-directing S···*M* noncovalent semicoordination bonding